THz Analysis of $CH_3NH_3PbI_3$ Perovskites Associated with Graphene and Silver Nanowire Electrodes

Zhi-Wei Huang,[1] Yu-Heng Hong,[1] Yi-Jheng Du,[1] Ting-Jui Kuo,[1] Chung-Che Huang,[2] Tsung Sheng Kao,[1] and Hyeyoung Ahn[1*]*

[1]Department of Photonics, College of Electrical and Computer Engineering, National Chiao Tung University, Hsinchu 30010, Taiwan.

[2]Optoelectronics Research Centre, University of Southampton, Southampton SO17 1BJ, UK.

KEYWORDS. hybrid organic–inorganic perovskites, terahertz spectroscopy, silver nanowire bottom electrode, graphene top electrode, tetragonal-to-cubic phase transition, Al_2O_3 layer

ABSTRACT. In order to investigate the thermal and chemical (in)stabilities of $MAPbI_3$ incorporated with graphene and silver nanowire (AgNW) electrodes, we employed the THz time-domain spectroscopy (THz-TDS) which has a unique ability to deliver the information of electrical properties and the intermolecular bonding and crystalline nature of materials. In *in situ* THz spectroscopy of $MAPbI_3$, we observed a slight blue-shift in frequency of 2-THz phonon mode as temperatures increase across the tetragonal-cubic structural phase transition. For $MAPbI_3$ with the graphene top electrode, no noticeable frequency shift is observed until the temperature reaches the maximum operating temperature of solar cells (85 ℃). Phonon frequency shift is sensitive to the

strain-induced tilt of PbI_6 octahedra and our results indicate that graphene forms a stable interface with $MAPbI_3$ and is also effective in suppression of the undesirable phase transition. Meanwhile, for $MAPbI_3$ coupled with the AgNW bottom electrode, the THz conductivity was found to be as low as that of $MAPbI_3$ single layer, attributed to the chemical reaction between Ag atoms and iodide ions. The THz conductivity is greatly increased when an ultrathin Al_2O_3 interlayer is introduced to cover the AgNW network via the atomic layer deposition (ALD) method. ALD of Al_2O_3 on the AgNW surfaces at low temperature guarantees a conformal coating which strongly affects the ohmic contacts between the NWs. Our results demonstrate the advantage of THz spectroscopy for the comprehensive analysis of thermal and chemical stabilities of perovskites associated with the electrode materials.

1. Introduction

Hybrid organic–inorganic halide (OIH) perovskites, such as methylammonium lead iodide ($MAPbI_3$) perovskite, have exhibited remarkable optical and electrical properties such as broad solar absorption and excellent charge transport for solar cells.[1,2] Despite the recent conversion efficiency exceeding 25 %,[3] the intrinsic degradation of OIH perovskites can be proceeded under ambient conditions, raising questions about the actual device performance.[4-6] Meanwhile, in the vertically integrated composite devices, another crucial instability can arise at the contact interface between different components. In particular, the transparent conductive electrodes (TCEs) in solar cells are in direct contact with the perovskite layer and their stabilities at the interface are vital in determination of the device performance. Recent emerging demands for reliable and flexible TCEs found that graphene and silver nanowires are very promising alternatives to replace indium tin oxide.[7-15] Besides its excellent conducting properties, many studies have also demonstrated that graphene electrode on the top of the $MAPbI_3$ layer (G/$MAPbI_3$) is beneficial in inhibiting the

octahedral tilt at the interface[16-18] and improving the thermal stability near the maximum device operating temperature (T_o~85 °C).[19-21] For the $MAPbI_3$ grown on AgNW network layer ($MAPbI_3$/AgNW), the chemical reaction between Ag atoms and iodide ions causes not only a serious degradation of the perovskite layer, but also reduction of electrical conductivity of the system.[6,22] Recently, intense efforts have been made to improve the interface stability between perovskites and metal electrodes for photovoltaic applications[23-25] and among them, the insertion of thin metal oxide (for example, Al_2O_3) layer is proved to be effective in preventing the ion diffusion and chemical reaction between adjacent layers.[26-28]

Full characterization of the different nature of interface stabilities requires a combination of several experimental techniques. Among them, the infrared/Raman spectroscopy is frequently used to realize the structural transition and vibration modes, but their sensitivity is greatly reduced in the low frequency ranges (<100 cm^{-1}).[29] The electrical properties of materials are typically determined using the direct contact methods, but these techniques are poorly suited for nanostructured materials. In this work, we employed a single experimental technique, terahertz time-domain spectroscopy (THz-TDS), to characterize two major stabilities of $MAPbI_3$; the thermal stability under the outdoor operating conditions and the chemical stability at the interface with metallic electrodes. Owing to the heavy atomic mass and the difference in the nature of bonding, the vibrational modes of I-Pb-I and Pb-I bonds in $MAPbI_3$ appear at around 1 and 2 THz, respectively.[30] Thus, THz-TDS with high sensitivity in the frequency range of 0.4 to 3 THz is particularly useful in phonon mode characterization of $MAPbI_3$. In addition, THz-TDS is a contact-free and optical method whose phase-sensitive technique enables the precise characterization of static electrical properties of materials, especially nanostructured materials. In our previous works, the strain-induced phonon splitting of $MAPbI_3$ and the thermal stability of hybrid G/AgNW

electrode have been explored by using THz-TDS.[31,32] Here, we extend the potential application of THz-TDS to provide insight of the stability at G/$MAPbI_3$ and $MAPbI_3$/AgNW interfaces.

For solar cells operating under long-term solar irradiation, the continuous heating may cause the thermal instability of devices. Especially for $MAPbI_3$-based solar cells, the tetragonal-cubic phase transition occurs at ~60-65 ℃ (T_c),[33-35] much lower that T_o. The phase transition is directly associated with the tilt of PbI_6 octahedra and in turn influences the phonon modes of $MAPbI_3$. In the *in-situ* measurement of THz-TDS, a slight blueshift in frequency of 2-THz phonon mode is observed as the temperature increases above T_c. Graphene has over 100-fold anisotropy of heat flow between the in-plane and out-of-plane directions[36] and G/$MAPbI_3$ does not show noticeable mode shift even at the temperature of 90 ℃, indicating the suppression of the undesirable phase transition and enhancement of thermal stability. This result is confirmed by the repeated THZ-TDS measurement for $MAPbI_3$ covered with molybdenum disulfide (MoS_2).

In the THz-TDS measurement of $MAPbI_3$/AgNW, we observed the complete vanishing of the continuous conducting path in the AgNW web and the THz conductivity shows a non-Drude frequency dependence. This result may be because during the solution process, the perovskite molecules may infiltrate into the gaps of AgNWs and accelerate the chemical reaction at NW junctions. When an ultrathin Al_2O_3 interlayer is introduced between $MAPbI_3$ and AgNW layers, the THz response of $MAPbI_3$/Al_2O_3/AgNW shows a typical Drude behavior with largely increased conductivity. Besides blocking the migration of Ag atoms, the Al_2O_3 interlayer conformally grown on the AgNW network is found to improve the NW junction contact.[37,38]

2. Results and Discussion

2-1. Thermal Stability of $MAPbI_3$ with Graphene Top Electrode

It has been reported that the structural as well as strain-induced phase transition of OIH perovskite is mainly driven by phonon modes associated with the inorganic lattice.[31,39] Vibrational modes of corner-sharing octahedral networks mainly appear in the low frequency (<5 THz) region due to their heavy atomic mass and are observed as resonance peaks in the THz spectra. In order to understand the details of vibrational modes in $MAPbI_3$ and their evolution process with thermal heating, the complex THz conductivities, $\tilde{\sigma}(= \sigma_1 + i\sigma_2)$, are measured *in-situ* for every 10 ℃-rise in temperature up to 90 ℃. Details concerning the THz data extraction and fitting processes have been previously reported elsewhere.[31] Figure 1a shows $\sigma_1(\omega)$ of the $MAPbI_3$ film measured as the temperature increases from 25 to 90 ℃. At low temperatures, there are two resonance peaks at ~1.6 (P_d) and 2 THz (P_1); P_1 corresponds to the Pb-I bending mode of tetragonal $MAPbI_3$ and P_d is typically related with the structural deformation in the disordered tetragonal phases.[39,40] As the annealing temperature increases above 60 ℃, P_d becomes relatively weaker than P_1 which becomes broader and increases in amplitude. The reduction of the defect-related P_d indicates that the disordered tetragonal perovskites may be transformed to the structurally ordered state by thermal annealing.

In addition to P_d, P_1 displays several interesting features. In Figure 1b, a detailed plot of $\sigma_1(\omega)$ on expanded scale near 2 THz shows that at temperatures below 60 ℃, there is a single peak centered at 2 THz, but at 60 ℃, a new small peak (P_2) emerges at 2.1 THz. Figure 1b and c also show that further increase in temperature results in the peak shifting towards higher frequencies and a considerable increase in strength of P_2. It is similar to the mode-split of $MAPbI_3$ at ~160 K, which is attributed to the orthorhombic-to-tetragonal phase transition.[41] In order to demonstrate that the observed blue-shift of phonon mode is due to the tetragonal-to-cubic phase transition in $MAPbI_3$, we repeated the same measurement for another OIH perovskite, $MAPbBr_3$,

which exists in the cubic phase at room temperature. Figure 1d shows that despite the increase in mode strength, there is no detectable frequency shift in the THz transmittance spectrum of $MAPbBr_3$ under annealing up to 90 ℃. Separately measured X-ray diffraction (XRD) curves in Figure S1 confirms the tetragonal-to-cubic phase transition.

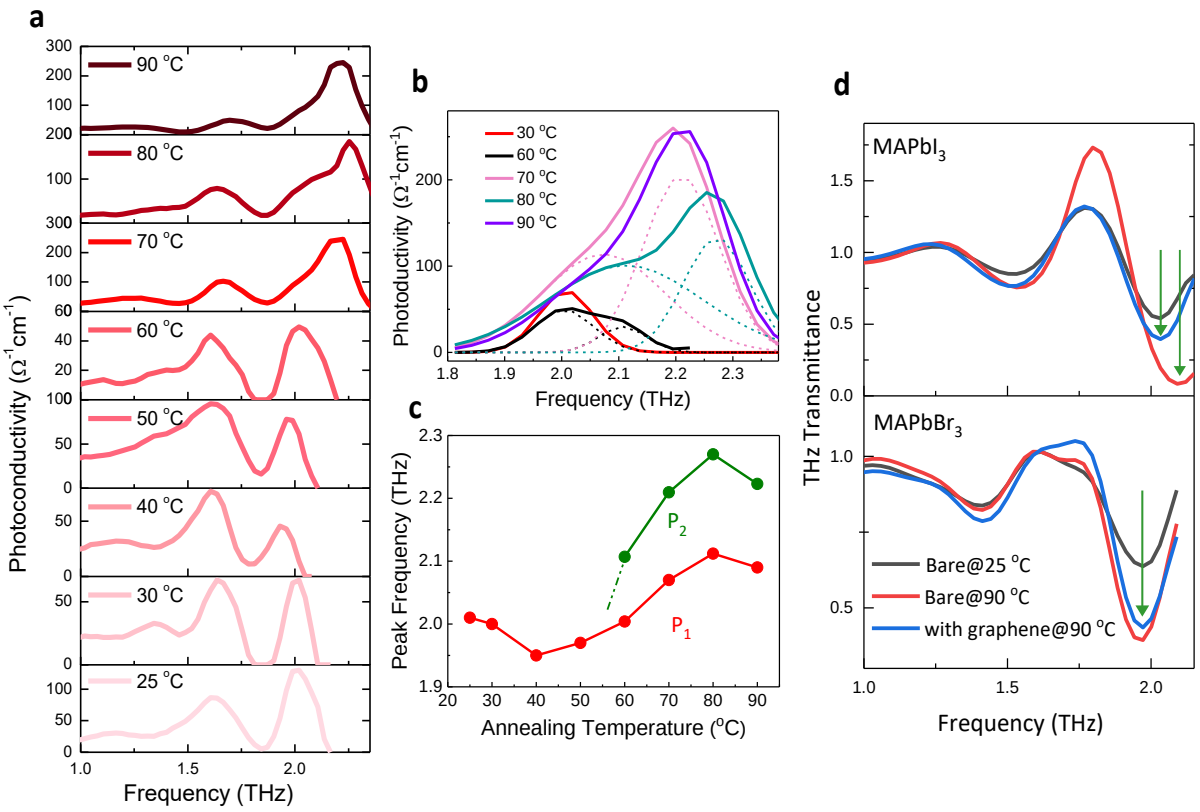

Figure 1. a. Temperature dependence of photoconductivity spectra of $MAPbI_3$ in the frequency range of 1.0-2.3 THz. Resonant peaks correspond to the vibration modes of mainly inorganic octahedra. **b.** Photoconductivity spectra and peak-fitting curves for the resonant phonon mode at ~2 THz. **c.** Frequency shift of P_1 and P_2 at different annealing temperatures. **d.** THz transmittance at 25 and 90 ℃ for $MAPbI_3$ and $MAPbBr_3$ with and without graphene overlayer.

Thermal-induced structural change of perovskites is known to be a surface-dominating sequential process, starting from the top surface and gradually propagating to underlayers.[42]

Graphene overlayer is known to suppress the octahedral tilt in the interface with the perovskite film.[16] Then, if the top surface of perovskite is covered by a highly conductive and hydrophobic graphene, the thermal and ambient stabilities of perovskites are expected to be significantly improved.[16,43] Previously, a large increase of T_c has been reported for the perovskite film coated with ZnO nanoshell, in which the interfacial-field-induced atomic rearrangement is suppressed by ZnO overlayer.[44] To control the phase transition in a similar way, we utilized large-area graphene monolayers to cover the surface of $MAPbI_3$ and $MAPbBr_3$, and investigated the thermal stability by using the THz-TDS measurement.[45,46] In Figure 1d, the phase shift-induced blue-shift of phonon mode is no longer observed for the graphene-covered $MAPbI_3$ (G/$MAPbI_3$) film annealed at 90 ℃. It indicates that graphene monolayer can effectively suppress the structural deformation of inorganics cages and increase the critical temperature for phase transition beyond the maximum device operating temperature. For cubic phase $MAPbBr_3$, little change is observed for G/$MAPbBr_3$ with thermal heating up to 90 ℃. It is noteworthy to mention that the mode frequency is not altered by the presence of graphene top layer on both $MAPbI_3$ and $MAPbBr_3$, implying that graphene/perovskite interface is stable in octahedral tilt.

Other two-dimensional materials such as MoS_2 have also been known to be effective for interface stability of perovskites.[47-50] MoS_2 is a semiconducting 2D material and due to its larger lattice constant (3.12 Å) than graphene (2.45 Å) and anisotropic lattice orientation,[51] their interaction with perovskites can be different from G/$MAPbI_3$.[50] Figure 2a shows that the phonon mode of MoS_2/$MAPbI_3$ appears at a shorter frequency ~1.9 THz than G/$MAPbI_3$, implying stronger effect of surface strain. Figure 2a also shows that there is no further phase-transition-related blue-shift on temperature increase above T_c, confirming the enhanced thermal stability of MoS_2/$MAPbI_3$. Interestingly, the THz spectra in Figure 2b show that the MoS_2 monolayer on the

top of $MAPbBr_3$ induces a red-shift in phonon frequency, in contrast to the blue-shift for $MoS_2/MAPbI_3$. This may be attributed to the lattice mismatching between MoS_2 and perovskites with different lattice constants,[52] illustrating the superior sensitivity of THz spectroscopy in analysis of the vibrational modes of OIH perovskites.

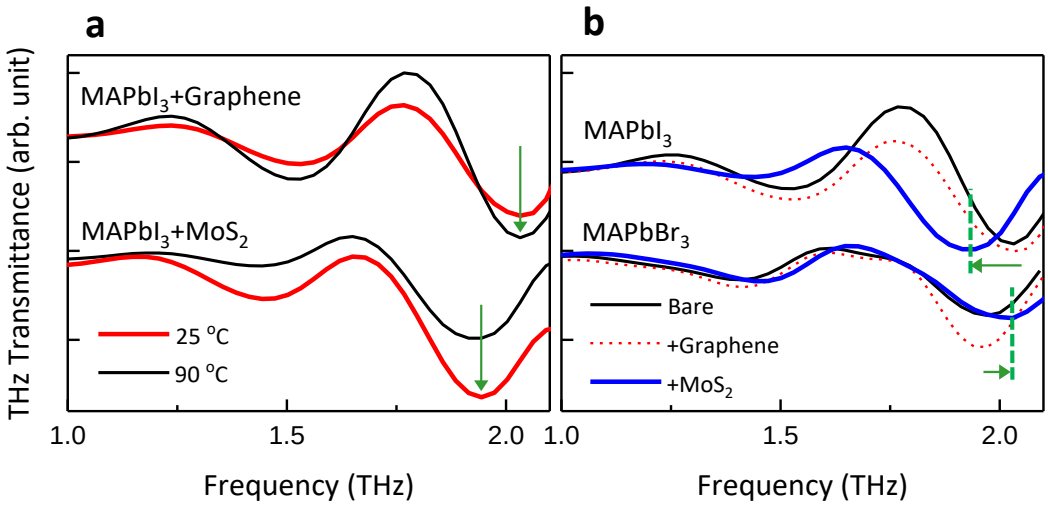

Figure 2. a. THz transmittance at 25 and 90 ℃ of $MAPbI_3$ covered by graphene and MoS_2 compared with that of $G/MAPbI_3$. **b.** THz transmittance spectra of $MAPbI_3$ and $MAPbBr_3$ covered with MoS_2 compared with those of $G/MAPbI_3$ and $MAPbI_3$ single layer.

2-2. Chemical Stability of $MAPbI_3$ on Silver Nanowire Bottom Electrodes

Despite high flexibility and conductivity, unprotected AgNW networks may induce significant chemical instability in the $MAPbI_3$ and AgNW hybrid system due to their high diffusivity and chemical reactivity with halide elements.[53] We investigated the degradation of $MAPbI_3$ due to chemical instability by THz spectroscopy in combination of several experimental methods. Firstly, Figure 3 shows the XRD curves of $MAPbI_3$/AgNW and the $MAPbI_3$ single layer directly fabricated on quartz substrate ($MAPbI_3$/Q). For $MAPbI_3$/AgNW, besides the XRD peaks indexed with those in tetragonal phase $MAPbI_3$, there are two additional peaks; one at 23.7° corresponding to AgI

(JCPDS No. 09-0399) (111) and the other at 32.9° belonging to Ag_2O (JCPDS 43-0997), providing a clear evidence of Ag atom diffusion to the perovskite layer. Another diffraction peak at ~12.6° corresponding to PbI_2 residue in perovskite film is noticeably larger for $MAPbI_3$/AgNW than that for $MAPbI_3$/Q, confirming the chemical reaction of iodide ions with diffused Ag atoms.

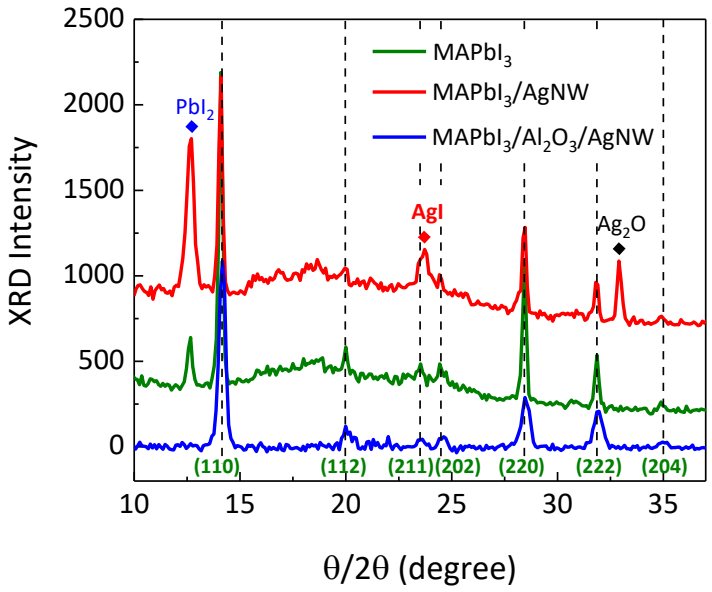

Figure 3. X-ray diffraction curves of $MAPbI_3$/Q, $MAPbI_3$/AgNW, and $MAPbI_3/Al_2O_3$/AgNW. The indexed peaks in $MAPbI_3/Al_2O_3$/AgNW are for tetragonal phase $MAPbI_3$. Two peaks at 23.7° and 32.9° for $MAPbI_3$/AgNW correspond to AgI and Ag_2O, respectively. The peak at 12.6° indicates the residual PbI_2. The figures are vertically shifted for clear presentation.

As an effort to prevent Ag atom diffusion, an ultrathin Al_2O_3 layer is deposited on the AgNW networks by ALD technique.[54] Due to its insulating nature, the thickness of Al_2O_3 layer is kept below 5 nm for the sufficient charge transfer to the perovskite layer. Table S1 shows the electrical conductivity of AgNWs covered by different thicknesses of Al_2O_3 layer. Figure 3 also exhibits the XRD curve of $MAPbI_3$ films fabricated on Al_2O_3-protected AgNWs ($MAPbI_3/Al_2O_3$/AgNW). Apparently, diffraction peaks corresponding to AgI and Ag_2O are absent

in the $MAPbI_3/Al_2O_3$/AgNW system, demonstrating that Ag atom diffusion can be effectively blocked by the Al_2O_3 layer. Furthermore, the peak of PbI_2 is also not observed in $MAPbI_3/Al_2O_3$/AgNW, implying that ALD-grown Al_2O_3 interlayer supports the formation of high quality tetragonal $MAPbI_3$.[55]

Next, we measured $\sigma_1(\omega)$ of $MAPbI_3$ incorporated with the AgNW bottom electrode using THz-TDS method and the results are shown in Figure 4. In our previous works, THz spectroscopy has been utilized to evaluate the AgNW networks near the percolation threshold and the influence of oxidation and thermal annealing of G/AgNW.[31,32] The AgNW layer with NW concentration (>0.15 wt %) forms a conductive network with high DC conductivity (ω= 0 Hz).[32] Interestingly, Figure 4 shows that when the unprotected AgNWs are incorporated with $MAPbI_3$, the THz response of $MAPbI_3$/AgNW is nearly the same as that of $MAPbI_3$ single layer, indicating the vanishing of the continuous conducting paths in the AgNW web after deposition of $MAPbI_3$ layer. Here, we need to emphasize that the $MAPbI_3$ layers were deposited simultaneously on three different substrates (bare quartz, AgNW/quartz, and Al_2O_3/AgNW/quartz) to ensure the same quality and thickness of perovskite layer and the THz measurement was performed within a few hours after deposition. Therefore, the observed similar responses between $MAPbI_3$/Q and $MAPbI_3$/AgNW may indicate that during the solution process, the perovskite may infiltrate into the gaps of AgNWs and react with Ag atoms, causing the disconnection of percolation path in AgNW networks.

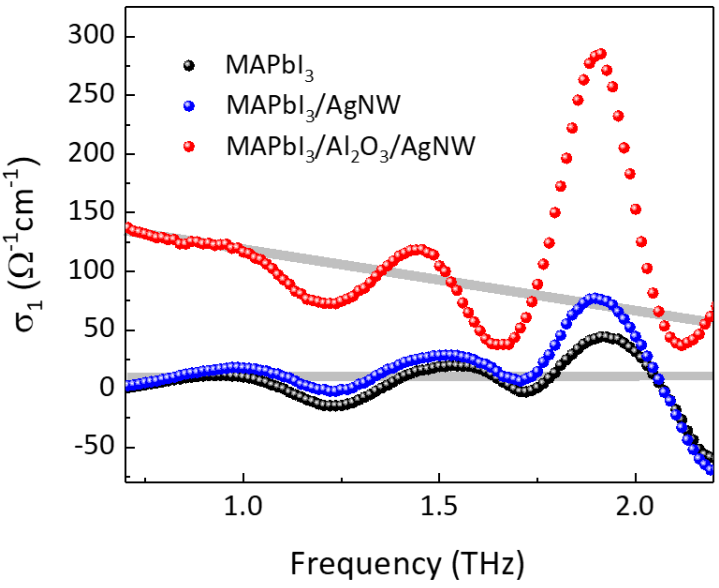

Figure 4. $\sigma_1(\omega)$ of $MAPbI_3$ single layer, $MAPbI_3$/AgNW, and $MAPbI_3/Al_2O_3$/AgNW. Solid curves are obtained by using the simple Drude model (for $MAPbI_3/Al_2O_3$/AgNW) and the Drude-Smith model[56] (for $MAPbI_3$ single layer and $MAPbI_3$/AgNW) with fitting parameters of the plasma frequency and the carrier scattering time in Table S2.

Meanwhile, for $MAPbI_3/Al_2O_3$/AgNW, $\sigma_1(\omega)$ illustrates a clear Drude-like dependence on frequency with the estimated DC conductivity of ~200 $\Omega^{-1}cm^{-1}$ (ω= 0 Hz), which is much higher than that (~13 $\Omega^{-1}cm^{-1}$) of $MAPbI_3$/AgNW. (see Table S2) Percolatively connected AgNW networks can maintain its high conductivity only up to ~200 ℃ and above that, melting and breakage of NW junctions cause the serious degradation of performance.[31] In order to avoid the melting of AgNWs during the ALD process, the deposition temperature of Al_2O_3 film was kept below 150 ℃, but this temperature is high enough to improve the contact of NW junctions through the removal of the polyvinylpyrrolidone capping layer on AgNW.[31] Therefore, the improvement of junction connectivity of Al_2O_3/AgNW leads to the enhancement of photoconductivity of $MAPbI_3/Al_2O_3$/AgNW hybrid system. In addition, the strength of phonon mode at ~2 THz in

$MAPbI_3/Al_2O_3/AgNW$ is largely enhanced compared to that in $MAPbI_3/AgNW$, implying the formation of better quality perovskites on the ALD-deposited thin Al_2O_3 films. The Al_2O_3 encapsulating layer also improves the surface roughness of AgNW layer originating from the pentagonal shape of NWs and their random distribution and enables the homogeneous growth of perovskite layer.[57]

Figure 5 depicts the structural configurations and element distribution with the cross-sectional TEM images of $MAPbI_3/Al_2O_3/AgNW$. A single pentagonal AgNW of diameter ~120 nm covered by the perovskite layer can be clearly observed in a dark-field image in Figure 5a. Figure 5b-d show the energy dispersive X-ray spectroscopy (EDX) mapping of atomic elements, Ag, Al, and I. Apparently, ultrathin Al_2O_3 interlayer conformally covers the surface of AgNWs, and Ag elements are not observed in the perovskite layer. Meanwhile, for $MAPbI_3/AgNW$, no AgNW is found in TEM images covering the area of at least 10 μm, which is much larger than the average space (≤5 μm) between NWs. (see **Figure S1**) This may be due to the decomposition of the unprotected AgNWs[58] and is consistent with the result of THz-TDS in Figure 4. Figure S1 also shows that the $MAPbI_3$ perovskite layer in the $MAPbI_3/AgNW$ system is composed of closely-packed large (~200 nm) grains of perovskite, whereas the perovskite layer in $MAPbI_3/Al_2O_3/AgNW$ is smooth and continuous without any vertically running grain boundary.

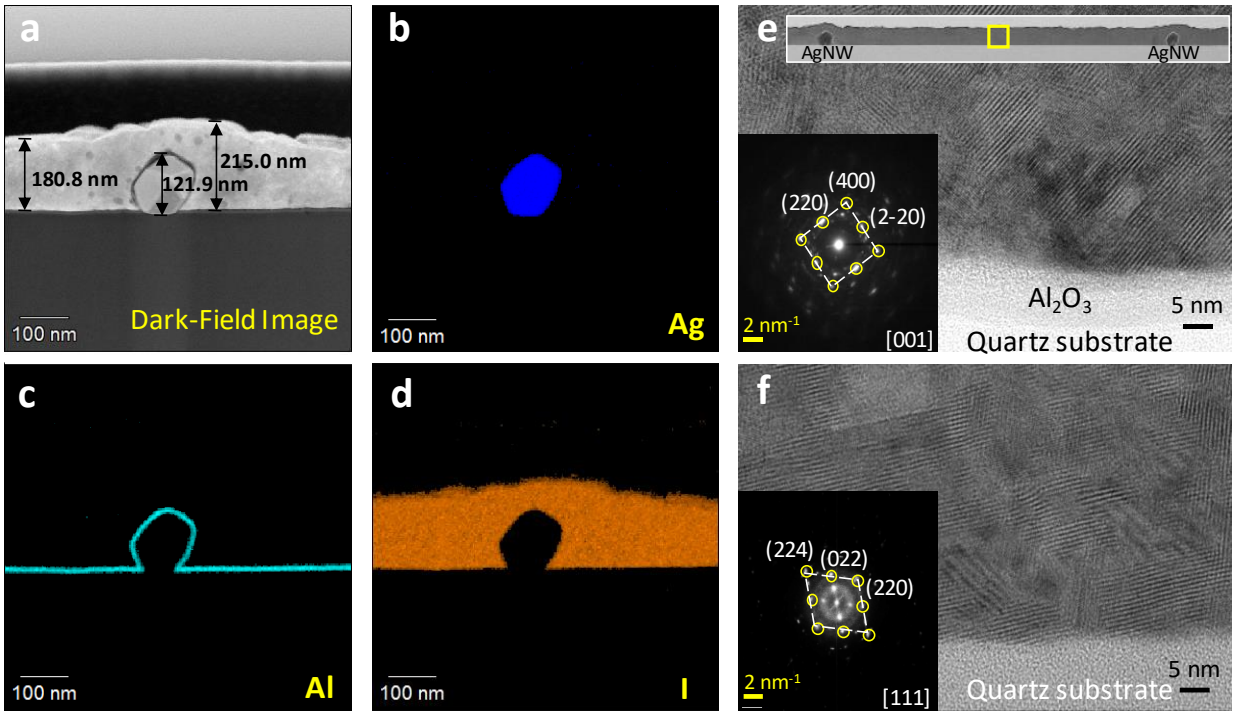

Figure 5. a. Cross-sectional TEM dark-field image of $MAPbI_3/Al_2O_3/AgNW$. **b-d.** The EDX mapping images corresponding to Ag, Al, and I atoms. **e,f**. HR-TEM images of $MAPbI_3/Al_2O_3/AgNW$ and $MAPbI_3/AgNW$. Insets show the SAED patterns and circles correspond to diffraction spots of tetragonal phase $MAPbI_3$.

In Figure 5e, the high-resolution TEM (HR-TEM) image of the $MAPbI_3/Al_2O_3/AgNW$ structure (taken in the yellow square area between AgNWs) shows the high-crystalline quality $MAPbI_3$ layer with excellent texture. The *d*-spacings determined from selected area electron diffraction (SAED) measurements in the inset of Figure 5e allow indexing of the diffraction spots for tetragonal $MAPbI_3$ pattern along the [001] axis. In Figure 5f, the HR-TEM image of $MAPbI_3/AgNW$ is shown and the corresponding SAED image in the inset exhibits a weak ring pattern overlapped with clear diffraction spots, which is typically appeared for relatively lower crystalline quality films. This result is consistent with the findings of XRD measurements in Figure 3.

3. Conclusions

In this article, we report on the experimental investigation by THz time-domain spectroscopy of $MAPbI_3$ incorporated with graphene top electrode and AgNW bottom electrode. Vibrational modes of $MAPbI_3$ have fingerprint features in the THz spectral range and they are sensitive to the surface and interface quality. Temperature-dependent THz spectroscopy reveals that a new phonon mode emerges upon heating above 60 ℃, which is associated with the structural phase transition from tetragonal phase into cubic phase. Incorporation with two-dimensional materials, such as graphene and MoS_2, is found to be beneficial not only in formation of stable interface, but also in effective dissipation of solar heating to suppress the phase transition during the outdoor operation of $MAPbI_3$-based solar cells. The THz conductivity spectroscopy on $MAPbI_3$ incorporated with AgNW bottom electrodes shows that the conductivity of AgNW film, especially at NW junctions, are significantly affected by the chemical reaction between Ag atoms and iodide ions. Chemically stable interface as well as the high-quality crystal growth can be achieved by covering AgNW film with an ultrathin Al_2O_3 layer. This study demonstrated the potential and unique applications of THz spectroscopy in simultaneous evaluation of the phonon modes and electrical properties of organic-inorganic hybrid perovskites incorporated with different electrodes. It also provided the evidences of improved chemical and thermal stabilities of perovskites, paving a route of non-contact diagnosis for device performance improvements in practical applications.

Experimental Section

Fabrication Procedures for Solution-processed Metal-halide Perovskites. The procedures of perovskite fabrication involve the anti-solvent technique using a solvent-engineered precursor solution, which consists of a γ-butyrolactone (GBL) and dimethyl sulfoxide (DMSO) mixture. The powdered lead (II) iodide (PbI_2) and methylammonium iodide (MAI) are dissolved in the prepared

precursor solution with the 1 molar (M) concentration. The as-prepared solution is deposited onto substrates by a consecutive two-stage spin-coating process at 1000 rpm and 5000 rpm for 10 and 50 seconds, respectively. During the second spin-coating stage, a dripping of anti-solvent toluene is continuously dripped onto the 15×15 mm^2 quartz substrates. Finally, the resulting thin films are annealed at 100 ℃ for 30 minutes to remove the residual solvents and transit the intermediate solvate phase into the perovskite, generating the $MAPbI_3$ perovskite films. All of the fabrications are carried out inside a nitrogen-filled glove box at room temperature.

Fabrication Procedures for Perovskite-AgNW Hybrid Structures. AgNW films with high NW concentrations are prepared by using the spin coating method on quartz substrates. Typical concentration of AgNWs used for this work is ~0.15 wt%, which is much higher than the percolation threshold (~0.10 wt%) of conductive AgNW networks.[32] AgNWs dispersed in isopropyl alcohol are acquired from Seashell Technology, LLC (AgNW-60) with an average diameter of 120-150 nm and a length of 10 μm. Films of different densities are fabricated by subsequent dilution to proper concentration with the same solvent. A micropipette is used to drop 50 μL of the AgNW suspension on the Si substrates and then spun-cast at 1200 rpm for 40 s, followed by heating to 90 ℃ for 3 min to vaporize any residual solvent. 5 nm-thick Al_2O_3 is deposited through atomic layer deposition to avoid degradation of AgNWs.

Fabrication and transfer of graphene and MoS_2 layers. A typical chemical vapor deposition (CVD) system was exploited for the fabrication of graphene. In the fabrication process, a 25-μm Cu foil substrate was cleaned and loaded into the CVD system. The Cu foil was annealed at 1000 ℃ with 6% H_2/Ar gas flow of 100 sccm for 30 min. The graphene growth was performed by flowing 5% CH_4/Ar together with 6% H_2/Ar gases for 20 mins with the flow rates of 100 sccm

and 210 sccm respectively. The size of the as-grown graphene layer may be up to around 80 mm × 90 mm, while the quality of the fabricated graphene was characterized by Raman spectroscopy. To transfer the graphene layer onto the perovskite thin films, the CVD-grown graphene on Cu foil was spin-coated with 7% polystyrene (PS, Sigma-Aldrich) in toluene at the speed of 1000 rpm for 50 secs, and then cured on a hot plate at 90 ℃ for 15 min. After removing the Cu foil through etching, the coated sample was subsequently attached with a supporting frame made with thermal release (TR) tape (from Nitto). Then the TR frame/PS/graphene/Cu was immersed in a 0.2M ammonium persulfate solution to etch away Cu foil. After that, TR frame/PS/graphene was rinsed with DI water and dried naturally in the air. Finally, the TR frame/PS/graphene was ready for transfer on perovskite/quartz and then the TR frame was released by baking at 110 ℃ for 30 mins. The mobility and carrier concentration of monolayer graphene measured by Hall measurement are 1680±378 $cm^2/V/s$ and $(8.4\pm2.9)\times10^{12}$ cm^{-2}.[59] MoS_2 monolayer was fabricated by Van der Waals Epitaxy (VdWE). The VdWE-grown MoS_2 monolayer on quartz substrate was spin-coated with 7% polystyrene (PS, Sigma-Aldrich) in toluene at the speed of 1000 rpm for 50 s, and then cured on a hot plate at 90 ℃ for 15 min. The coated sample was subsequently attached with a supporting frame made with TR tape. Then the TR frame/PS/MoS_2/quartz was immersed in the DI water to allow water to penetrate through the Van der Waals gap between MoS_2 and the quartz substrate. After that, TR frame/PS/MoS_2 was floating on the DI water and then further rinsed with DI water and dried naturally in the air. Finally, the TR frame/PS/MoS_2 was ready for transfer on Perovskite/quartz and then the TR frame was released by baking at 110 ℃ for 30 mins.

Characterization System The morphologies of perovskite films are analyzed by using field-emission scanning electron microscopy (FE-SEM, Zeiss-Ultraplus). The THz conductivities of $MAPbI_3$ films are measured using the THz time-domain spectroscopy (THz-TDS) technique. Our

homemade THz-TDS system is based on THz emission from a photoconductive antenna (Batop GmbH). The normally transmitted THz pulses were detected by free-space electro-optic sampling technique with a 2-mm-thick ZnTe crystal (EKSMA Optics), where the Pockels effect due to the THz field rotates the polarization of the sampling laser pulses.[60] A balanced detector detects the differential photocurrent as a function of delay time with respect to the optical pump pulse at 800 nm. All the measurements were done under dry nitrogen purge. The excitation of antenna and the probe of the THz signal through electro-optic sampling method are achieved with a Ti:sapphire laser (Coherent Chameleon Ultra II) which delivers ~150 fs optical pulses at a center wavelength of 800 nm. For post-annealing measurement, samples are sandwiched by a pair of commercially available mini electrical ceramic heat-plate (with a 5×5 mm^2 square hole at the center) and the sample temperature is controlled and measured by thermocouple during the in-situ THz-TDS measurement. In THz-TDS analysis, the THz wave spectra are obtained by the application of a fast Fourier transform to the time-domain waveforms for both the substrate and the film on the substrate. Dividing the spectrum obtained from the perovskite film on the substrate by that obtained with the substrate yields the magnitude and phase difference of the complex transmission amplitude of the perovskite layer. From the Fourier transforms (power spectra and phase shifts), we can determine the frequency-dependent photoconductivities as well as the dielectric constants of the perovskite samples. XRD θ-2θ scans (Bede D1 HR-XRD) of perovskite films are performed using an XRD diffractometer with monochromatic Cu-Kα radiation (λ = 1.5406 Å) to characterize the reflections along the surface normal.

Associated Content

Supporting Information. XRD curves of $MAPbI_3$ measured at room temperature and after annealing at 90 ºC. (Figure S1) TEM image of $MAPbI_3$/AgNWs and $MAPbI_3/Al_2O_3$/AgNW systems. (Figure S2) Al_2O_3 thickness dependence of electrical conductivity of Al_2O_3/AgNW. (Table S1) The best fit parameters for the analysis of photoconductivity spectra in Figure 3. (Table S2) The Supporting Information is available free of charge.

Author Information

Corresponding Author

* Tel) +886-3-5712121-56332, Fax) +886-3-5716631, E-mail) tskao@nctu.edu.tw

* Tel) +886-3-5712121-56369, Fax) +886-3-5716631, E-mail) hyahn@mail.nctu.edu.tw

Author Contributions

H.A. and T.K. conceived and planned the experiments, and wrote the manuscript. Z.H. prepared AgNW network and conducted THz spectroscopy measurement. Y.D. and T.K. performed the optical experiments. Y.H. prepared perovskite samples. C.C. fabricated the graphene and MoS_2 layers and performed dry-transfer on perovskite thin films. All authors have given approval to the final version of the manuscript.

Funding Sources

This work has been financially supported by the Ministry of Science and Technology (MOST 107-2112-M-009-015-MY3 and MOST 107-2923-M-009-003-MY3, and MOST 107-2221-E-009-116-MY3) of Taiwan and the Future Photonics Manufacturing Hub (EPSRC EP/N00762X/1) and the Chalcogenide Photonic Technologies (v) at University of Southampton, United Kingdom.

Abbreviations

$MAPbI_3$, methylammonium lead iodide; AgNW, silver nanowire; ALD, atomic layer deposition; OIH, organic–inorganic halide; THz-TDS, terahertz time-domain spectroscopy; AgI, silver iodide; Al_2O_3, aluminum oxide; G/$MAPbI_3$, graphene-covered $MAPbI_3$; $MAPbI_3$/AgNW, $MAPbI_3$ on AgNW layer; $MAPbI_3$/Q, $MAPbI_3$ on quartz substrate; XRD, X-ray diffraction; TEM, transmission electron microscope; EDX, energy dispersive X-ray spectroscopy; SAED, selected area electron diffraction; PL, photoluminescence.

References

1. Lee, M. M.; Teuscher, J.; Miyasaka, T; Murakami, T. N; Snaith, H. J. Efficient Hybrid Solar Cells Based on Meso-Superstructured Organometal Halide Perovskites. *Science*, **2012**, *338*, 643–647.

2. Gao, P.; Grätzel M. Nazeeruddin M. K. Organohalide Lead Perovskites for Photovoltaic Applications. *Energy Environ. Sci*., **2014**, *7*, 2448–2463.

3. https://www.nrel.gov/pv/assets/pdfs/best-research-cell-efficiencies.20190923.pdf.

4. Wang, Z.; Shi, Z.; Li, T.; Chen, Y.; Huang, W. Stability of Perovskite Solar Cells: A Prospective on the Substitution of the A Cation and X Anion. *Angew. Chem., Int. Ed.* **2016**, *56*, 1190–1212.

5. Niu, G.; Guo, X.; Wang, L. Review of Recent Progress in Chemical Stability of Perovskite Solar Cells. *J. Mater. Chem. A*, **2015**, *3*, 8970–8980.

6. Boyd, C. C.; Cheacharoen, R.; Leijtens, T.; McGehee, M. D. Understanding Degradation Mechanisms and Improving Stability of Perovskite Photovoltaics. *Chem. Rev.* **2019**, *119*, 3418−3451.

7. Wassei, J. K.; Kaner, R. B. Graphene, a Promising Transparent Conductor. Mater. Today **2010**, *13*, 52–59.

8. Pang, S. P.; Hernandez, Y.; Feng, X. L.; Müllen, K. Graphene as Transparent Electrode Material for Organic Electronics. *Adv. Mater.* 2011, *23*, 2779– 2795.

9. Park, H.; Brown, P. R.; Bulović, V.; Kong, J. Graphene As Transparent Conducting Electrodes in Organic Photovoltaics: Studies in Graphene Morphology, Hole Transporting Layers, and Counter Electrodes. *Nano Lett.* **2012**, *12*, 133–140.

10. Hecht, D. S.; Hu, L. B.; Irvin, G. Emerging Transparent Electrodes Based on Thin Films of Carbon Nanotubes, Graphene, and Metallic Nanostructures. *Adv. Mater.* **2011**, *23*, 1482–1513.

11. Sun Y.; Xia Y. Large-Scale Synthesis of Uniform Silver Nanowires Through a Soft, Self-Seeding, Polyol Process. *Adv. Mater.* (*Weinheim, Ger.*) **2002**, *14*, 833–837.

12. Yeh, M.-H.; Chen, P.-H.; Yang, Y.-C.; Chen, G.-H.; Chen, H.-S. Investigation of Ag-TiO_2 Interfacial Reaction of Highly Stable Ag Nanowire Transparent Conductive Film with Conformal TiO_2 Coating by Atomic Layer Deposition. *ACS Appl. Mater. Interfaces* **2017**, *9*, 10788−10797.

13. Chen, D.; Liang, J.; Liu, C.; Saldanha, G.; Zhao, F.; Tong, K.; Liu, J.; Pei, Q. Thermally Stable Silver Nanowire-Polyimide Transparent Electrode Based on Atomic Layer Deposition of Zinc Oxide on Silver Nanowires. *Adv. Funct. Mater.* **2015**, *25*, 7512−7520.

14. Yan, X.; Ma, J.; Xu, H.; Wang, C.; Liu, Y. Fabrication of Silver Nanowires and Metal Oxide Composite Transparent Electrodes and Their Application in UV Light-Emitting Diodes. *J. Phys. D: Appl. Phys.* **2016**, *49*, 325103.

15. Su, D.-Y.; Hsu, C.-C.; Lai, W.-H.; Tsai, F.-Y. Fabrication, Mechanisms, and Properties of High-Performance Flexible Transparent Conductive Gas-Barrier Films Based on Ag Nanowires and Atomic Layer Deposition. *ACS Appl. Mater. Interfaces* **2019**, *11*, 34212−34221.

16. Volonakis G.; Giustino, F. Ferroelectric Graphene−Perovskite Interfaces. *J. Phys. Chem. Lett.* **2015**, *6*, 2496−2502.

17. Wang W-W, Dang J-S, Jono R, Segawa H and Sugimoto M 2018 A first-principles prediction on 'healing effect' of graphene preventing carrier trapping near the surface of metal halide perovskites Chem. Sci. 9 3341–53.

18. Di Carlo, A.; Agresti, A.; Brunetti, F.; Sara Pescetelli, S. Two-Dimensional Materials in Perovskite Solar Cells *J. Phys. Energy* 2020, *2*, 031003.

19. Leijtens, T.; Bush, K.; Cheacharoen, R.; Beal, R.; Bowring, A.; McGehee, M. D. Towards Enabling Stable Lead Halide Perovskite Solar Cells; Interplay between Structural, Environmental, and Thermal Stability. *J. Mater. Chem. A* **2017**, *5*, 11483.

20. Ava, T. T.; Mamun, A. A.; Marsillac, S.; Namkoong, G. A Review: Thermal Stability of Methylammonium Lead Halide Based Perovskite Solar Cells. *Appl. Sci*. **2019**, *9*, 188.

21. Quarti, C.; Mosconi, E.; Ball, J. M.; D'Innocenzo, V.; Tao, C.; Pathak, S.; Snaith, H. J.; Petrozza, A.; Angelis, F. D. Structural and Optical Properties of Methylammonium Lead Iodide across the Tetragonal to Cubic Phase Transition: Implications for Perovskite Solar Cells. *Energy Environ. Sci.* **2016**, *9*, 155–163.

22. Fu, Q.; Tang, X.; Huang, B.; Hu, T.; Tan, L.; Chen, L.; Chen, Y. Recent Progress on the Long-Term Stability of Perovskite Solar Cells. *Adv. Sci*. **2018**, *5*, 1700387.

23. Lu, H.; Sun, J.; Zhang, H.; Lu, S.; Choy, W. C. H. Room-Temperature Solution-Processed and Metal Oxide-Free Nano-Composite for the Flexible Transparent Bottom Electrode of Perovskite Solar Cells. *Nanoscales,* **2016**, *8,* 5946–5953.

24. Lu, H.; Ren, X.; Ouyang, D.; Choy, W. C. H. Emerging Novel Metal Electrodes for Photovoltaic Applications. *Small,* **2018**, *14*, 1703140.

25. Kim, J.; Ouyang, D.; Lu, H.; Ye, F.; Guo, Y.; Zhao, N.; Wallace C. H. Choy, W. C. H. High Performance Flexible Transparent Electrode via One-Step Multifunctional Treatment for Ag Nanonetwork Composites Semi-Embedded in Low-Temperature-Processed Substrate for Highly Performed Organic Photovoltaics. *Adv. Energy Mater.,* **2020**, *10,* 1903919.

26. Cao, B.; Yang, L.; Jiang, S.; Lin, H.; Wang N.; Li, X. Flexible Quintuple Cation Perovskite Solar Cells with High Efficiency. *J. Mater. Chem. A,* **2019**, *7*, 4960–4970.

27. Lee, Y. H.; Luo, J.; Son, M.-K.; Gao, P.; Cho, K. T.; Seo, J. ; Zakeeruddin, S. M.; Grätzel, M.; Nazeeruddin, M. K. Enhanced Charge Collection with Passivation Layers in Perovskite Solar Cells. *Adv. Mater*. **2016**, *28*, 3966–3972.

28. Poodt, P.; Lankhorst, A.; Roozeboom, F.; Spee, K.; Maas, D.; Vermeer, A. High-Speed Spatial Atomic-Layer Deposition of Aluminum Oxide Layers for Solar Cell Passivation. *Adv. Mater.,* **2010**, *22*, 3564–3567.

29. Kojima, S.; Mori, T.; Shibata, T.; Kobayashi, Y. Broadband Terahertz Time-Domain and Low-Frequency Raman Spectroscopy of Crystalline and Glassy Pharmaceuticals. *Pharm. Anal. Acta* **2015**, *6*, 1000401.

30. Quarti, C.; Grancini, G.; Mosconi, E.; Bruno, P.; Ball, J. M.; Lee, M. M.; Snaith, H. J.; Petrozza, A.; Angelis, F. D. The Raman Spectrum of the $CH_3NH_3PbI_3$ Hybrid Perovskite: Interplay of Theory and Experiment. *J. Phys. Chem. Lett.* **2014**, *5*, 279–284.

31. Chen, J.-Z.; Ahn, H.; Yen, S.-C.; Tsai, Y.-J. Thermally Induced Percolational Transition and Thermal Stability of Silver Nanowire Networks Studied by THz Spectroscopy. *ACS Appl. Mater. Interfaces* **2014**, *6*, 20994−20999.

32. Tsai, Y.-J.; Chang, C.-Y.; Lai, Y.-C.; Yu, P.-C.; Ahn, H. Realization of Metal-Insulator Transition and Oxidation in Silver Nanowire Percolating Networks by Terahertz Reflection Spectroscopy," *ACS Appl. Mater. Interfaces*, **2014**, *6*, 630−635.

33. Milot, R. L.; Eperon, G. E.; Snaith, H. J.; Johnston, M. B.; Herz, L. M. Temperature-Dependent Charge-Carrier Dynamics in $CH_3NH_3PbI_3$ Perovskite Thin Films. *Adv. Funct. Mater.* **2015**, *25*(39), 6218–6227.

34. Saidi W. A.; Choi, J. J. Nature of the Cubic to Tetragonal Phase Transition in Methylammonium Lead Iodide Perovskite. *J. Chem. Phys*. **2016**, *145*, 144702.

35. Whitfield, P. S.; Herron, N.; Guise, W. E.; Page, K.; Cheng, Y. Q.; Milas, I.; Crawford, M. K. Structures, Phase Transitions and Tricritical Behavior of the Hybrid Perovskite Methyl Ammonium Lead Iodide. *Sci. Rep*. **2016**, *6*, 35685.

36. Pierson, H. O. Handbook of Carbon, Graphite, Diamond and Fullerenes: Properties, Processing and Applications (Noyes Publications, Park Ridge, NJ , 1993).

37. Ali, K.; Duraisamy, N.; Kim, C. Y.; Choi, K.-H. Al_2O_3 Coatings Fabrication on Silver Nanowires through Low Temperature Atomic Layer Deposition. *Mater. Manuf. Processes* **2014**, *29*, 1056−1061.

38. Dong, Q.; Liu, F.; Wong, M. K.; Tam, H. W.; Djurišić, A. B.; Ng, A.; Surya, C.; Chan, W. K.; Ng, A. M. C. Encapsulation of Perovskite Solar Cells for High Humidity Conditions. *ChemSusChem* **2016**, *9*, 2597–2603.

39. Ahn, H.; Huang, H.; Hsieh, M.-I.; Li, M. H.; Chen, P. Observation of Strain-Induced Phonon Mode Splitting in the Tetragonal Hybrid Halide Perovskite. *Jpn. J. Appl. Phys.* **2017**, *56*, 110307.

40. Maeng, I.; Lee, Y. M.; Park, J.; Raga, S. R.; Kang, C.; Kee, C,-S.; Yu, B. D.; Hong, S.; Ono, L. K.; Qi, Y.; Jung, M.-C.; Nakamura, M. Significant THz Absorption in CH_3NH_2 Molecular Defect-Incorporated Organic-Inorganic Hybrid Perovskite Thin Film. *Sci. Rep.* **2019** *9*, 5811.

41. La-o-vorakiat, C.; Xia, H.; Kadro, J.; Salim, T.; Zhao, Z.; Ahmed, T.; Lam, Y. M.; Zhu, J.-X.; Marcus, R. A.; Michel-Beyerle, M.-E.; Chia, E. E. M. Phonon Mode Transformation Across the Orthohombic−Tetragonal Phase Transition in a Lead Iodide Perovskite $CH_3NH_3PbI_3$: A Terahertz Time-Domain Spectroscopy Approach. *J. Phys. Chem. Lett.* **2016**, *7*, 1−6.

42. Christians, J. A.; Miranda Herrera, P. A.; Kamat, P.V. Transformation of the Excited State and Photovoltaic Efficiency of $CH_3NH_3PbI_3$ Perovskite upon Controlled Exposure to Humidified Air. *J. Am. Chem. Soc*. **2015**, *137*, 1530–1538.

43. Hu, X.; Jiang, H.; Li, J.; Ma, J.; Yang, D.; Liu, Z.; Gao, F.; Liu, S. F. Air and Thermally Stable Perovskite Solar Cells with CVD-Graphene as the Blocking Layer, *Nanoscale* **2017**, *9*, 8274−8280.

44. Zhao, F.; Gao, X.; Fang, X.; Glinka, Y. D.; Feng, X.; He, Z.; Wei, Z.; Chen, R. Interfacial-Field-Induced Increase of the Structural Phase Transition Temperature in Organic–Inorganic Perovskite Crystals Coated with ZnO Nanoshell. *Adv. Mater. Interfaces* **2018**, *5*, 1800301.

45. Lin, H.; Song, Y.; Huang, Y.; Kita, D.; Deckoff-Jone, S.; Wang, K.; Li, L.; Li, J.; Zheng, H.; Luo, Z.; Wang, H.; Novak, S.; Yadav, A.; Haung, C.-C.; Shiue, R.-J.; Englund, D.; Gu, T.; Hewak D.; Richardson, K.; Kong, J.; Hu J. Chalcogenide Glass-on-Graphene Photonics, *Nat. Photonics* **2017**, *11*, *798–805*.

46. Zhang, H.; Healy, N.; Shen, L.; Huang, C.-C.; Hewak, D.W.; Peacock, A.C. Enhanced All-optical Modulation in a Graphene-coated Fibre with Low Insertion Loss, *Sci. Rep.* **2016**, *6,* 23512.

47. Fan, Z.; Xiao, H.; Wang, Y.; Zhao, Z.; Lin, Z.; Cheng, H.-C.; Lee, S.-J.; Wang, G.; Feng, Z.; Goddard, W. A. III; Huang, Y.; Duan, X. Layer-by-Layer Degradation of Methylammonium Lead Tri-Iodide Perovskite Microplates. *Joule* **2017**, *15*, 1–15.

48. Peng, B.; Yu, G.; Zhao, Y.; Xu, Q.; Xing, G.; Liu, X. Fu, D.; Deng, L.; Sum, T. C.; Loh, K. P.; Liu, B.; Tan, J. R. S.; Tang, W.; Lu, H.; Xie, J. Achieving Ultrafast Hole Transfer at the Monolayer MoS_2 and $CH_3NH_3PbI_3$ Perovskite Interface by Defect Engineering, *ACS Nano* **2016**, *10*, 6383–6391.

49. Kakavelakis, G; Paradisanos, I.; Paci, B.; Generosi, A.; Papachatzakis, M.; Maksudov, T.; Najafi, L.; Del Rio Castillo, A. E.; Kioseoglou, G.; Stratakis, E.; Bonaccorso, F.; Kymakis, E. Extending the Continuous Operating Lifetime of Perovskite Solar Cells with a Molybdenum Disulfide Hole Extraction Interlayer. *Adv. Energy Mater.* **2018**, *8*, 1702287.

50. Di Carlo, A.; Agresti, A.; Brunetti, F.; Sara Pescetelli, S. Two-Dimensional Materials in Perovskite Solar Cells *J. Phys. Energy* **2020**, *2*, 031003.

51. Ma, Y.D.; Dai, Y.; Guo, M.; Niu, C.W.; Huang, B.B. Graphene Adhesion on MoS_2 Monolayer: An ab initio Study. *Nanoscale* **2011**, *3*, 3883–3887.

52. Wang, L.; King, I.; Chen, P.; Bates, M.; Lunt, R. R. Epitaxial and Quasiepitaxial Growth of Halide Perovskites: New Routes to High End Optoelectronics. *APL Mater.* **2020**, *8*, 100904.

53. Rhead, G. E. Surface Self-Diffusion of Silver in Various Atmospheres. *Acta Metallurgica* **1965**, *13*, 3223–3226.

54. Hwang, B.; An, Y.; Lee, H.; Lee, E.; Becker, S.; Kim, Y.-H.; Kim, H. Highly Flexible and Transparent Ag Nanowire Electrode Encapsulated with Ultra-Thin Al_2O_3: Thermal, Ambient, and Mechanical Stabilities. *Sci. Rep.* **2017**, *7*, 41336.

55. Zhang, J.; Hultqvist, A.; Zhang, T.; Jiang, L.; Ruan, C.; Yang, L.; Cheng, Y.; Edoff, M.; Johansson, E. M. J. Al_2O_3 Underlayer Prepared by Atomic Layer Deposition for Efficient Perovskite Solar Cells. *ChemSusChem* **2017**, *10*, 3810–3817.

56. Smith, N.V. Classical Generalization of the Drude Formula for the Optical Conductivity. *Phys. Rev. B* **2001**, *64*, 155106–4.

57. Yoo, J. H.; Kim, Y.; Han, M. K.; Choi, S.; Song, K. Y.; Chung, K. C.; Kim, J. M.; Kwak, J. Silver Nanowire−Conducting Polymer−ITO Hybrids for Flexible and Transparent Conductive Electrodes with Excellent Durability. *ACS Appl. Mater. Interfaces* **2015**, *7*, 15928−15934.

58. Lee, E.; Ahn, J.; Kwon, H.-C.; Ma, S.; Kim, K.; Yun, S.; Moon, J. All-Solution-Processed Silver Nanowire Window Electrode Based Flexible Perovskite Solar Cells Enabled with Amorphous Metal Oxide Protection. *Adv. Energy Mater*. **2017**, *8*, 1702182.

59. Lin , H; Song, Y.; Huang, Y.; Kita, D.; Deckoff-Jones, S.; Wang, K.; Li, L.; Li, J.; Zheng, H.; Luo, Z.; Wang, H.; Novak, S.; Yadav, A.; Huang, C.-C.; Shiue, R.-J.; Englund, D.; Gu, T.; Hewak, D.; Richardson, K.; Kong, J.; Hu, J. Chalcogenide Glass-on-Graphene Photonics. *Nat. Photonics*, **2017**, *11*, 798–805.

60. Ahn, H; Pan, C.-L.; Gwo, S. Terahertz Emission and Spectroscopy on InN Epilayer and Nanostructure. *Proc. of SPIE* **2009**, *7216*, 72160T.

Table of Contents graphic